



# Bonding CdS-Sn<sub>2</sub>S<sub>3</sub> eutectic clusters on graphene nanosheets with unusually photoreaction-driven structural reconfiguration effect for excellent H<sub>2</sub> evolution and Cr(VI) reduction

Chao Xue, Xiaoqing Yan, Hua An, He Li, Jinjia Wei, Guidong Yang\*

*XJTU-Oxford International Joint Laboratory for Catalysis, School of Chemical Engineering and Technology, Xi'an Jiaotong University, Xi'an, 710049, China*

## ARTICLE INFO

### Keywords:

Graphene  
CdS-Sn<sub>2</sub>S<sub>3</sub>  
Reconfiguration  
Active sites  
Photocatalysis

## ABSTRACT

In this work, a novel CdS-Sn<sub>2</sub>S<sub>3</sub>@reduced graphene oxide (rGO) eutectic cluster heterostructures were synthesized via a facile one-pot hydrothermal method, which can make CdS-Sn<sub>2</sub>S<sub>3</sub> uniformly dispersed onto the rGO nanosheets surface and thus form a specially active sites sustained-release tablets. The optimized sample displayed continuously increased visible-light-driven photocatalytic activity and strong durability both in photocatalytic hydrogen evolution and hexavalent chromium (Cr(VI)) reduction. With these results, we for the first time find the peculiarly structural reconfiguration effect produced in the CdS-Sn<sub>2</sub>S<sub>3</sub>@rGO composite, and the reaction-driven reconfiguring of graphene-based CdS-Sn<sub>2</sub>S<sub>3</sub> eutectics can act as sustained-release system of active sites, which triggers incomparable merits, such as more active sites, shorter charge-transfer distance and the effective interfacial contact. In addition, the rGO nanosheets served as electron shuttle to efficiently accelerate the separation and transfer of photogenerated electron-hole pairs. These combined effects endowed the hybrids system with the ever-increasing hydrogen-generating efficiency and enhanced stability in reduction reaction.

## 1. Introduction

In past decades, a “bottom-up” approach is frequently employed to provide insights into surface dynamics, adsorption-desorption processes and the possible reaction pathways during the heterogeneous catalytic processes with a fixed solid catalyst surface structure [1–4]. However, in many cases, the geometric structure and composition of surfaces are easily to be altered during the realistic catalytic reaction, which results in the conventional analysis models are usually simplified. Recent studies demonstrate that structural reconstructions of nanostructured materials not only tailor the size and morphology of the catalytic particles, but also reconstruct the surface events or even subsurface regions [3]. This reconfiguration in their spatial architecture can trigger some of advanced functions of catalysts. For example, (i) The size and morphology of the nano-scaled materials can change drastically in response to changing reaction environment [5]. Especially, the larger particles can break up into the smaller ones accompanying with internal reconfigurations, which not only change the electronic properties of the surface, but also significantly increase the specific surface area of catalysts, thus exposing a large number of surface active sites. (ii) The surfaces reconstructions will alter subsurface of materials to reach the thermodynamic equilibrium under reaction conditions [4]. Meanwhile,

some composition of the constituent elements may migrate from bulk or deep layers of subsurface regions to the top surface layer and continuously create new active sites for participating in various heterogeneous catalytic reactions [6].

Given the favorable attributes, the structural reconfiguration of nano-architectures is a versatile implementation strategy to develop visible-light-driven photocatalysts for solar-induced photoelectric or photochemical conversion of hydrogen, which is also considered to be a promising route in response to challenging energy crises and environmental issues [7–11]. Therefore, tremendous efforts have been devoted to prepare highly-efficient photocatalytic systems and uncover the involved reaction mechanism. However, as far as we know, almost all the existing research focuses on the improvement of the photocatalytic performance by bandgap engineering [12], surface and interface design [13], dye sensitization [14], or exploring novel semiconductors with narrow bandgap [15]. Once these architected semiconductors were synthesized, they still possess a fixed geometric morphology that cannot be reconfigured leading to a limited practicability in photocatalysis.

Pioneering attempts have demonstrated that two dimensional (2D) graphene is an attractive host matrices which can provides an ideal platform for the design of reconfigurable systems, owing to its structural flexibility, large specific surface area and outstanding conductivity

\* Corresponding author.

E-mail address: [guidongyang@xjtu.edu.cn](mailto:guidongyang@xjtu.edu.cn) (G. Yang).

and electron mobility [16–18]. Inspired by the merits of reconfigurability, in this work, we for the first time fabricated a novel CdS-Sn<sub>2</sub>S<sub>3</sub>@rGO eutectic cluster heterostructures via the facile hydrothermal method. Compared to the traditional graphene-based hybrids, this ingenious CdS-Sn<sub>2</sub>S<sub>3</sub>@rGO heterostructures could in-situ reconfigure their spatial architecture and in this way to significantly improve the visible light photocatalytic activities and durability for H<sub>2</sub> evolution and Cr(VI) reduction. Furthermore, our findings provide a novel insight into the interplay of structure and photocatalytic properties of CdS-Sn<sub>2</sub>S<sub>3</sub>@rGO photocatalytic system. We believe that these architecture strategies provide the possibility to resolve the current bottlenecks about activity and durability reported in previous graphene-based metal sulfide photocatalysts.

## 2. Experimental section

### 2.1. Materials

Glucose (C<sub>6</sub>H<sub>12</sub>O<sub>6</sub>), cadmium chloride hemi(pentahydrate) (CdCl<sub>2</sub>·2.5H<sub>2</sub>O), tin tetrachloride pentahydrate (SnCl<sub>4</sub>·5H<sub>2</sub>O), L-cysteine (C<sub>3</sub>H<sub>7</sub>NO<sub>2</sub>S) were purchased from Sinopharm Chemical Reagent Co., Ltd. All the chemical reagents were analytical grade and used as-received.

### 2.2. The exfoliation of graphene oxide (GO)

The GO was synthesized by the modified Hummers' method. In order to obtain the highest-quality monolayer graphene nanosheets, the as-prepared GO were further treated by the ultrasonic-assisted exfoliation procedure. In brief, 60 mg of GO was added to 20 mL of deionized water. The mixture was transferred into an incubator at 0 °C and treated by sonication for about 6 h, forming a dark brown suspension with a concentration of 3 mg mL<sup>-1</sup>.

### 2.3. Synthesis of hybrid CdS-Sn<sub>2</sub>S<sub>3</sub>@rGO eutectic cluster heterostructure

The hybrid CdS-Sn<sub>2</sub>S<sub>3</sub>@rGO eutectic cluster heterostructures were synthesized using a facial one-pot hydrothermal method. In a typical procedure, 4 mL of the as-obtained GO (3 mg mL<sup>-1</sup>) suspension was dispersed in 30 mL of deionized water under the ultrasonication for 5 min. Then 0.2 g of glucose, 0.2307 g of CdCl<sub>2</sub>·2.5H<sub>2</sub>O and 0.1052 g SnCl<sub>4</sub>·5H<sub>2</sub>O were added into the aforementioned mixture under vigorous stirring for 4 h, followed by the addition of 0.59 g of L-cysteine. After being stirred for extra 1 h, the homogeneous suspension was transferred into a 100 mL Teflon-lined stainless autoclave and maintained at 180 °C for 2 h before cooling down to room temperature. The final products were collected by centrifugation, washed with distilled water and absolute ethanol several times, and vacuum-dried for 12 h at 60 °C for further characterization. A series of graphene-based metal sulphides heterostructure with the different molar ratio of Cd to Sn were fabricated via the above procedure by controlling the concentration of CdCl<sub>2</sub>·2.5H<sub>2</sub>O and SnCl<sub>4</sub>·5H<sub>2</sub>O. For comparison, the pristine CdS and Sn<sub>2</sub>S<sub>3</sub> were synthesized under the same conditions without adding GO, respectively.

### 2.4. Characterization

The crystal structure of samples was investigated using X-ray diffraction (XRD; SHIMADZU, Lab X XRD-6100) with Cu-Kα radiation at a scan rate of 10° min<sup>-1</sup>. X-ray photoelectron spectra (XPS) were carried out on AXIS ULTRABLD apparatus to examine the elemental compositions and chemical valence state of the as-prepared samples in the near-surface range. The morphologies and nanostructures of all the samples were accomplished by field-emission scanning electron microscopy (FE-SEM; FEI Quanta F250, 200 kV) equipped energy dispersive X-ray spectroscopy (EDX) and electronic energy loss spectroscopy (EELS), as

well as transmission electron microscopy (TEM; JEOL, JEM-2100). The time-resolved photoluminescence spectra were recorded on a PTI Quanta Master 400 fluorescence spectrometer (HORIBA Scientific) with an excitation wavelength of 402 nm. A thermogravimetric analysis (TGA; Beijing Henven Scientific Instrument Factory; HTC-3) was performed to quantitatively investigate the thermal properties of the as-prepared samples. And the samples were heated from ambient temperature to 800 °C at a heating rate of 10 °C min<sup>-1</sup> under a N<sub>2</sub> atmosphere. The concentration of Cd<sup>2+</sup> in solution was measured by an inductively coupled plasma atomic emission spectroscopy (ICP; SHIMADZU Corp., Japan; ICPE-9000). A 75W Xenon lamp is used as the excitation source for steady state experiments. The photoluminescence (PL) spectra of the as-synthesized samples in the powder form were investigated at room temperature on FLS980 fluorescence spectrometer (Edinburgh Instruments) with an excitation wavelength of 325 nm.

### 2.5. Photoelectrochemical performance measurement

The photoelectrochemical measurements were recorded on an electrochemical workstation (CHI 760D Shanghai Chenhua) in a three-electrode system. The irradiation light source was a 300 W Xenon lamp (Nbet, HSX-F/UV300) equipped with an ultraviolet cut-off glass filter (λ > 420 nm). An Ag/AgCl electrode and a platinum wire were respectively used as the reference electrode, the counter electrode. A glassy carbon electrode tip (effective area: 0.076 cm<sup>2</sup>) modified with the prepared samples were served as the working electrode. All aforementioned electrodes were working in a 0.5 M Na<sub>2</sub>SO<sub>4</sub> aqueous solution as the electrolyte.

### 2.6. Photocatalytic activity measurement

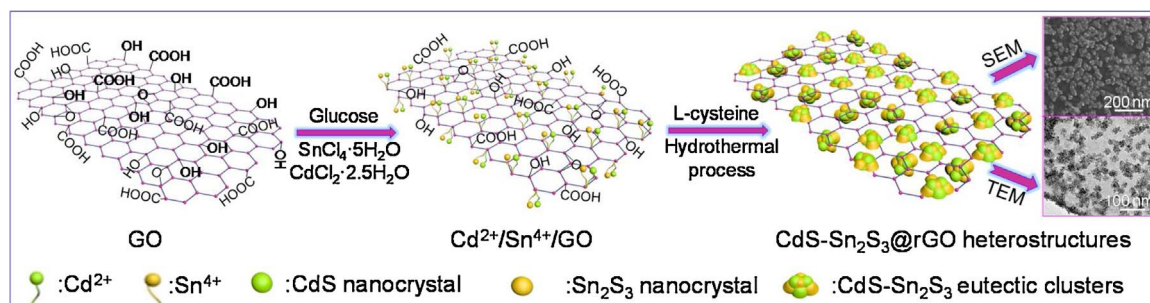
The photocatalytic tests of the prepared catalyst were performed by the reduction of K<sub>2</sub>Cr<sub>2</sub>O<sub>7</sub> aqueous solution (100 mg/L) under the visible light irradiation of a 300 W Xenon lamp (Nbet, HSX-F/UV300). Typically, 0.05 g photocatalyst and 0.03 g tartaric acid as hole sacrifice agent were adding into 50 mL 100 mg·L<sup>-1</sup> K<sub>2</sub>Cr<sub>2</sub>O<sub>7</sub> aqueous solution and the suspension was magnetically stirred in the dark for 60 min to obtain the adsorption-desorption equilibrium before the visible light illumination. During the reaction process, 3 mL of the suspension was taken out and centrifuged to isolate the photocatalyst at a certain time interval of 3 min, then the residual concentration of hexavalent chromium Cr(VI) was analyzed on a UV1900PPC spectrophotometer. The detection wavelength for the characteristic absorption peak of Cr(VI) is 350 nm. The cycling experiments were executed with the similar conditions except that the residual solution was analyzed after visible-light irradiation for 15 min.

### 2.7. Photocatalytic H<sub>2</sub> evolution

The photocatalytic H<sub>2</sub> evolution experiment was performed in a Pyrex reaction cell with a 300 W Xenon lamp (Nbet, HSX-F/UV300) as the visible light source. Typically, 0.5 g photocatalyst was dispersed in mixed solution containing 10 mL of lactic acid, 3 wt.% H<sub>2</sub>PtCl<sub>6</sub> and 50 mL of water with constant magnetically stirring. Prior to visible illumination, the system was degassed with nitrogen for 30 min to guarantee that the reaction system was under anaerobic conditions. The amount of H<sub>2</sub> generated was analyzed by gas chromatography (BFRL, SP-2100A, Beijing, China).

## 3. Results and discussion

As iconically shown in Scheme 1, the ternary ultrafine CdS-Sn<sub>2</sub>S<sub>3</sub>@rGO eutectic cluster heterostructures were synthesized directly by facile one-pot hydrothermal process. Assisted by the mechanical exfoliation, GO nanosheets with multifunctional oxygenic groups almost uniformly dispersed in the mixed aqueous solutions containing different



**Scheme 1.** Schematic illustration of the integration of CdS-Sn<sub>2</sub>S<sub>3</sub> eutectic clusters with GO nanosheets.

concentrations of tin ions (Sn<sup>4+</sup>) and cadmium ions (Cd<sup>2+</sup>) precursors. Meanwhile, plentiful positively charged metallic ions can be easily fixed by anchoring sites on the surface of electronegative GO nanosheets, and subsequently reacted with S<sup>2-</sup> released from L-cysteine, during the hydrothermal process. The nucleation and self-growth of CdS and Sn<sub>2</sub>S<sub>3</sub> were simultaneously occurred along with the reduction of GO. It's worth noting that the introduction of glucose not only effectively prevent the agglomeration of CdS-Sn<sub>2</sub>S<sub>3</sub> eutectic clusters but also act as a suitable reductant for GO reduction. Experimental details are elucidated in the experimental section. In this work, the molar ratios of CdS to cocatalyst Sn<sub>2</sub>S<sub>3</sub> were fixed at 4:3 and 8:3, and the resulted hybrid nanostructures were labeled as CGS-1 and CGS-2, respectively.

X-ray diffraction (XRD) gives the direct information about the crystal phase of as-synthesized pure and hybrid systems. As shown in Fig. 1a, the XRD patterns of CGS-1 and CGS-2 together with those of CdS/rGO (denoted as CG), Sn<sub>2</sub>S<sub>3</sub>/rGO (denoted as GS) as well as the pristine CdS and Sn<sub>2</sub>S<sub>3</sub> demonstrated the high crystallinity and all of the distinct diffraction peaks can be indexed to the hexagonal CdS (JCPDS 41-1049), and orthorhombic Sn<sub>2</sub>S<sub>3</sub> (JCPDS 14-0619), respectively.

Additionally, the structure was confirmed by Fourier transform infrared (FT-IR) spectroscopy, which would be discussed later.

Direct evidence for the immobilization of CdS and Sn<sub>2</sub>S<sub>3</sub> nanocrystals on rGO nanosheets can be observed from the field emission scanning electron microscopy (FESEM) and transmission electron microscopy (TEM). As indicated with arrowheads in Fig. S1 (Supporting information), the ultrathin GO nanosheets retain wrinkle shapes after ultrasonic exfoliation, which can not only prevent GO nanosheets from being restacked during the hydrothermal process, but also provide a high surface area for nucleating [16,17]. SEM images in Figs. S2, S3 (Supporting information) and Fig. 1 clearly show that the in-situ growth of single or binary metal sulfides on rGO nanosheets can efficiently prevent the aggregation of both rGO nanosheets and loaded metal sulfides, comparing to the pristine Sn<sub>2</sub>S<sub>3</sub> nanoparticles and CdS microspheres. As for CGS-2 composites (Fig. 1b and c), it's obvious that numerous island-like CdS-Sn<sub>2</sub>S<sub>3</sub> nanocrystals are homogeneously dispersed and tightly attached on rGO surface with a particle size of 16.7–27.8 nm. This structural characteristic of eutectic clusters gives rise to the possibility of reconfiguration on rGO surface. The edges of rGO

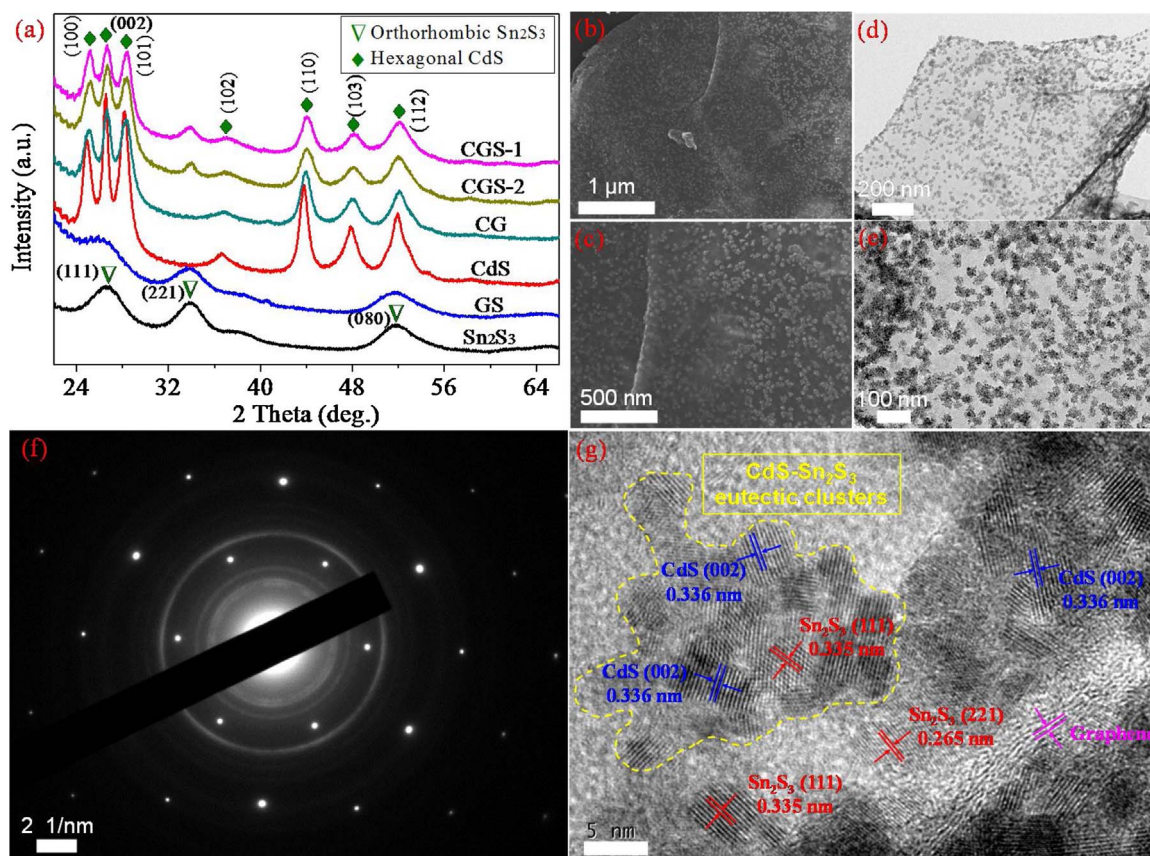


**Fig. 1.** (a) XRD patterns of all samples. (b,c) SEM images; (d,e) TEM images; (f) SAED pattern and (g) HRTEM images of CGS-2 composites.



nanosheets are clear in TEM images (Fig. 1d and e). It further confirmed that a dense mass of uniform and ultrafine CdS-Sn<sub>2</sub>S<sub>3</sub> eutectic clusters uniformly distributed on both sides of the rGO nanosheets, which could significantly augment the exposure area of active sites [18]. The selected area electron diffraction (SAED) pattern (Fig. 1f) indicates the polycrystalline nature of these eutectic clusters. Additionally, the distinct bright spots forming multiple sets of hexagons demonstrated a relatively highly ordered graphene structure and a regular stacking of few-layer rGO nanosheets in hybrid system [19,20]. A typical high-resolution TEM (HRTEM) image in Fig. 1g clearly reveal that CdS-Sn<sub>2</sub>S<sub>3</sub> eutectic clusters tightly anchored onto rGO surfaces to form the heterostructures with well-defined phase interfaces. The lattice fringes with d spacing of 0.335 and 0.265 nm can be assigned to the (111) and (221) planes of the cubic orthorhombic Sn<sub>2</sub>S<sub>3</sub>, respectively. It also presents well-defined hexagonal CdS nanocrystals with highly exposed (002) facets. Remarkably, the binary nanocrystals are intertwined together and established sufficient and stable interfacial connections with rGO nanosheets, which endow these unique ultrathin 2D nanosheets hybrids with superiority in shortening distance of charge transfer diffusion, improving interfacial charge transfer, suppressing charge recombination, and exposing more active sites for photoredox reaction.

X-ray photoelectron spectroscopy (XPS) spectra (Fig. S4, Supporting information) and elemental mapping images (Fig. S5, Supporting information) further evidenced the co-existence of the C, Cd, S, and Sn elements in the obtained CGS-2 sample. The high-resolution XPS spectrum of the O1s (Fig. S4c, Supporting Information) implies the partial residual of oxygen-involved functional groups and additional defects in surface of rGO. As manifested in Fig. S5d–f (Supporting Information), it is difficult to identify the clear boundaries of CdS and Sn<sub>2</sub>S<sub>3</sub> nanocrystals, attributing to their quite smaller sized architecture. Instead, we can reasonably draw a conclusion that the CdS-Sn<sub>2</sub>S<sub>3</sub> eutectic clusters were homogeneously distributed on the surface of the rGO nanosheets, resulting in an intimately interfacial contact.

Fig. 2a shows the Raman spectra of GO, CGS-1 and CGS-2 nanocomposite. Two distinct peaks located at 1345 cm<sup>-1</sup> and 1590 cm<sup>-1</sup>

can be clearly seen in Raman spectrum of GO, which correspond to the characteristic D and G bands, respectively [21,22]. By contrast, both CGS-1 and CGS-2 displayed D band at 1333 cm<sup>-1</sup> and G band at 1577 cm<sup>-1</sup>, respectively. The slight bands shift towards higher wavelength number indicated a significant electron transfer between the CdS-Sn<sub>2</sub>S<sub>3</sub> eutectic clusters and rGO nanosheets [23,24]. In addition, the relative intensity ratio of D to G band ( $I_D/I_G$ ) for CGS-2 composite was 1.23, which was higher than those of CGS-1 (1.18) and GO (1.03). The higher intensity ratios indicate the reduction of GO and the higher defect density in CGS-2 composite [25,26]. Notably, the existed defects can provide more active sites, which play a vital role for improving the photocatalytic activity [27]. Furthermore, significant changes also presented in FT-IR spectra (Fig. 2b). As compared to original GO, CdS-Sn<sub>2</sub>S<sub>3</sub>@rGO heterostructures exhibited much lower absorption intensity at the peaks assigned to the oxygen-containing functional groups, suggesting the successful reduction of GO to rGO via hydrothermal reduction process [20,26–28].

The UV–vis diffuse reflection spectra (DRS) (Fig. 2c) reflect that all as-prepared samples exhibited wide absorption in the ultraviolet and visible light region. Obviously, the combination of graphene has significantly expanded the absorption range of the ternary CdS-Sn<sub>2</sub>S<sub>3</sub>@rGO nanocomposites. Especially, the CGS-2 composite showed stronger visible light absorption than those of CG, CGS-1 composite and CdS. This enhanced light absorption property will lead to more efficient utilization of the solar energy for the CdS-Sn<sub>2</sub>S<sub>3</sub>@rGO composite system. Although Sn<sub>2</sub>S<sub>3</sub> exhibited the similar strong absorption intensity in visible light region, the photocurrent transient response of pure Sn<sub>2</sub>S<sub>3</sub> was negligible (Fig. 2d), implying the rapid recombination rate of photo-excited electron-hole pairs. It is noticeable that the initial value of photocurrent density for CG was as high as 58.5 μA cm<sup>-2</sup>, which was 21.2 times higher than that of single CdS. It indicates that the presence of rGO can favor the photo-induced electrons transfer from CdS to rGO nanosheets, thus improving the charge separation efficiency. However, an obviously photocurrent decay can be observed in CG with the increase of periodic illumination time, owing to the

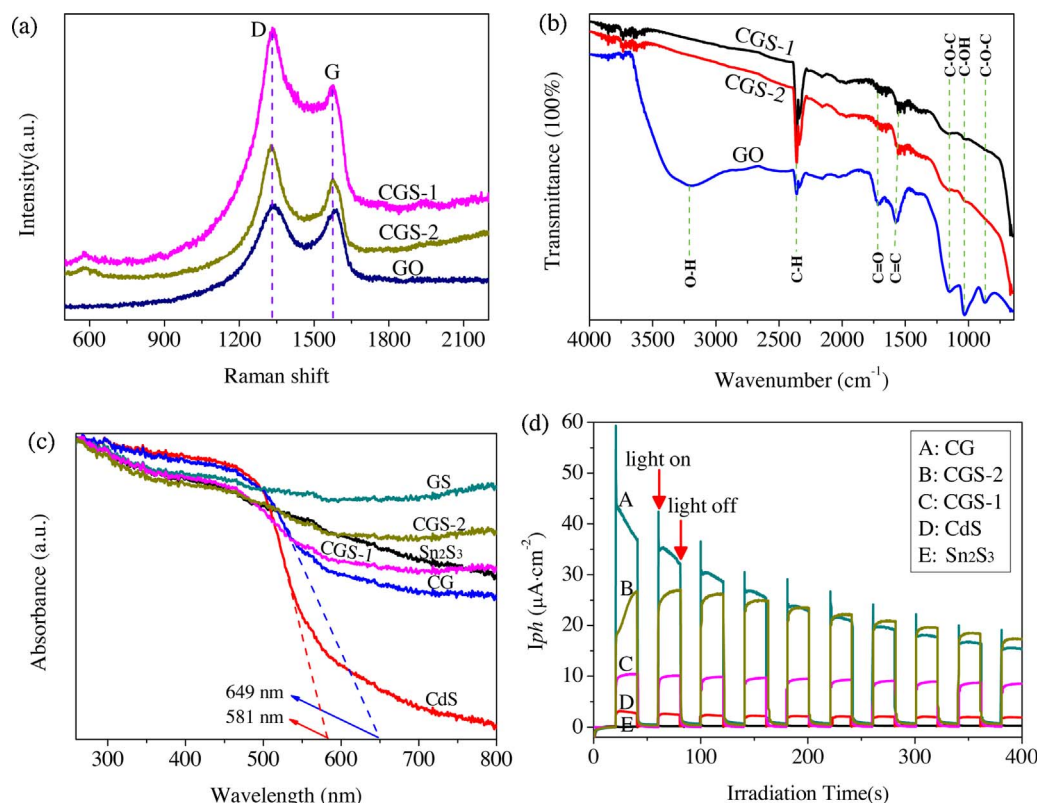


Fig. 2. (a) Raman spectra of GO, CGS-1 and CGS-2 excited at 633 nm; (b) FT-IR spectra, (c) UV–vis DRS spectra and (d) Transient photocurrent responses of as-fabricated samples.

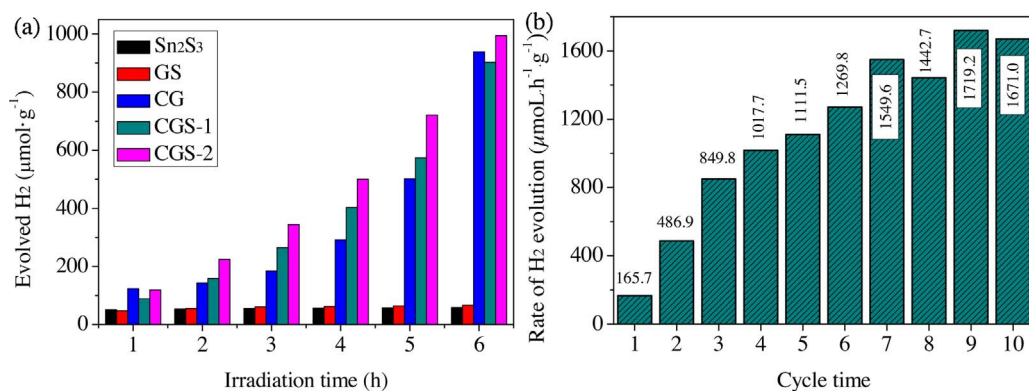


Fig. 3. (a) Time-resolved H<sub>2</sub> evolution over various photocatalysts under visible light irradiation and (b) Cycling test of H<sub>2</sub> evolution over CGS-2 composite (λ > 420 nm).

photocorrosion of CdS. In contrast, CdS-Sn<sub>2</sub>S<sub>3</sub>@rGO heterostructures exhibited better photocurrent stability than CG. The photocurrent density for CGS-2 and CGS-1 were highly reproducible for several on-off cycles and remained at 26.1 μA cm<sup>-2</sup> and 10.01 μA cm<sup>-2</sup>, respectively. This persistent stability further indicates that the integration of the constructed CdS-Sn<sub>2</sub>S<sub>3</sub> eutectic clusters heterojunction and rGO with superior electrical conductivity results in the lower recombination rate and the higher separation efficiency of photo-generated electron-hole pairs. A significant decrease of the PL intensity was observed in CGS-2 composites (Fig. S6, Supporting information), indicating slower recombination rate of photo-induced electron-hole pairs [21].

The photocatalytic properties of the as-synthesized photocatalysts were thoroughly investigated by photocatalytic hydrogen production under visible-light illumination (λ ≥ 420 nm) using 10 vol.% lactic acid aqueous solution as scavenger and 3 wt.% Pt as a co-catalyst. As depicted in Fig. 3a, the pure Sn<sub>2</sub>S<sub>3</sub> and GS showed the minimum photocatalytic activity because of the rapid recombination of photo-generated electron-hole pairs in direct band gap semiconductor Sn<sub>2</sub>S<sub>3</sub>. Under visible light irradiation for 6 h, the initial H<sub>2</sub> evolution rate of CGS-2 composite was reached up to 165.7 μmol h<sup>-1</sup> g<sup>-1</sup>, which was 1.1 and 1.0 times higher than that of CGS-1 and CG composites, respectively. It is surprising that the yield of H<sub>2</sub> over CGS-2 composite undergoes a continuous increase (Fig. 3b), and the H<sub>2</sub> evolution rate achieved the highest value of 1719.2 μmol h<sup>-1</sup> g<sup>-1</sup> after nine recycles. Even after cycles recycles, the nanohybrids did not show significant loss of activity, and the H<sub>2</sub> evolution rate retains at 1671.0 μmol h<sup>-1</sup> g<sup>-1</sup>. It indicates that the optimal ratio of Sn<sub>2</sub>S<sub>3</sub> imposed a significant influence on H<sub>2</sub> production activity of the CdS-Sn<sub>2</sub>S<sub>3</sub>@rGO eutectic cluster heterostructures [29,30]. And the optimized CGS-2 sample displayed good activity and stability in consecutive photocatalytic H<sub>2</sub> evolution process.

It is amazing that the resultant CGS-2 composites also displayed a better photocatalytic activity and excellent stability for Cr(VI) reduction. The detection wavelength for the characteristic absorption peak of Cr(VI) is 350 nm. As illustrated in Fig. 4a, the reduction of Cr(VI) hardly occurred in the absence of photocatalysts or in the presence of tartaric acid under visible light irradiation for 15 min. It is more convincing that CGS-2 displayed the highest photocatalytic activity with a reduction rate of 98.5%. While the removal efficiencies of Cr(VI) are only 90%, 76.5% and 28.9% over CGS-1, CG, and GS, respectively. Notably, both the pristine CdS and Sn<sub>2</sub>S<sub>3</sub> exhibited a similar low reduction ratio of Cr(VI) (approximately 50.7%) under the same conditions, due to the rapid recombination of photo-generated electron-hole pairs. As can be seen from Fig. S7, all the characteristic absorption peak of Cr(VI) over CGS-2 appear at 350 nm, and the characteristic absorption peak intensity of Cr(VI) was gradually decreased with the increase of irradiation time. Under visible light irradiation for 15 min, the characteristic absorption peak located at 350 nm disappeared, indicating that the heavy metal ions have been completely reduced during the photo-reduction process. As shown in Fig. 4b, the aforesaid photoreactions

followed a pseudo-first order dynamics model [31–34]. Significantly, the resultant CGS-2 possessed excellent stability and recyclability for photocatalytic reduction of Cr(VI). The removal efficiencies of Cr(VI) remain at 95.8% even in the tenth reuse cycle (Fig. 4d). This ternary CdS-Sn<sub>2</sub>S<sub>3</sub>@rGO eutectic cluster heterostructures show good potential in practical wastewater purification.

It is believed that the structural reorganization of CdS-Sn<sub>2</sub>S<sub>3</sub> eutectic clusters occurred on graphene nanosheets play a vital role for the ever-increasing photocatalytic H<sub>2</sub> evolution over CGS-2 composite. Comprehensive analysis of TEM and XRD convincingly verified the interplay between structure and photocatalytic activities. TEM images in Fig. 5 and Fig. S8 (Supporting information) revealed that dramatic change occurred in the whole morphology of CGS-2 composites at different reaction time. Compared with the original CGS-2 sample (Fig. 5a), the island-like CdS-Sn<sub>2</sub>S<sub>3</sub> eutectic clusters tended to self-disperse and converted into numerous ultrafine metal sulfides nanocrystals on rGO platform under the visible light irradiation. Particle sizes distributions determined by TEM present that the number of the large particles ranging from 10 to 30 nm decreased gradually with the increase of reaction time. On the contrary, the total number of smaller nanoparticles (concentrated on 2–3 nm in diameter) increased synchronously. Further observation revealed that the visualized CdS-Sn<sub>2</sub>S<sub>3</sub> eutectic clusters were completely collapsed after photocatalytic H<sub>2</sub> evolution for 6 h (Fig. 5m) or more (60 h, Fig. 5n). And newly formed nanocrystals were so tiny that it cannot be identified automatically by the software. HRTEM images in Fig. S8b and d (Supporting information) depict that the dissolved metal sulfide crystallites and in-situ reduced Pt nanoparticles densely anchored on the graphene nanosheets indicating an irreversible structural reconstruction of CdS-Sn<sub>2</sub>S<sub>3</sub>@rGO heterostructures during the photocatalysis process. The result of EDX spectrum (Fig. S8e; Supporting information) further confirmed that the metallic Pt<sup>0</sup> was successfully photo-deposited on the surface of CdS-Sn<sub>2</sub>S<sub>3</sub>@rGO nanocomposite during the photo-reduction process.

The surface elemental compositions and chemical states of the fresh CGS-2 sample and the used CGS-2 sample obtained after photocatalytic hydrogen evolution for 60 h were investigated by X-ray photoelectron spectroscopy (XPS) analysis. As demonstrated in Figs. S4a and S9a (Supporting Information), the whole XPS survey spectra showed that there are C, O, S, Cd and Sn elements coexist in the two samples. As shown in both the high-resolution C1s and O1s XPS spectra of the fresh CGS-2 sample and the used CGS-2 sample obtained after photocatalytic hydrogen evolution for 60 h (Fig. S4b,c and S9b, c), there are still some oxygen-containing functional groups in the CdS-Sn<sub>2</sub>S<sub>3</sub>@rGO heterostructures, indicating that the GO nanosheets was not completely reduced to the rGO nanosheets. Additionally, the two asymmetrical peaks located at 161.5 and 163.7 eV in the S 2p spectra can be ascribed to the S 2p<sub>3/2</sub> and S 2p<sub>1/2</sub> (Figs. S4d and S9d; Supporting information). As shown in Fig. S4e and Fig. S9e (Supporting Information), Cd 3d located at around 405.1 and 411.9 eV can be assigned to Cd 3d<sub>5/2</sub> and Cd 3d<sub>3/2</sub>, respectively. The Sn 3d spectra of the fresh CGS-2 sample (Fig. S4f;

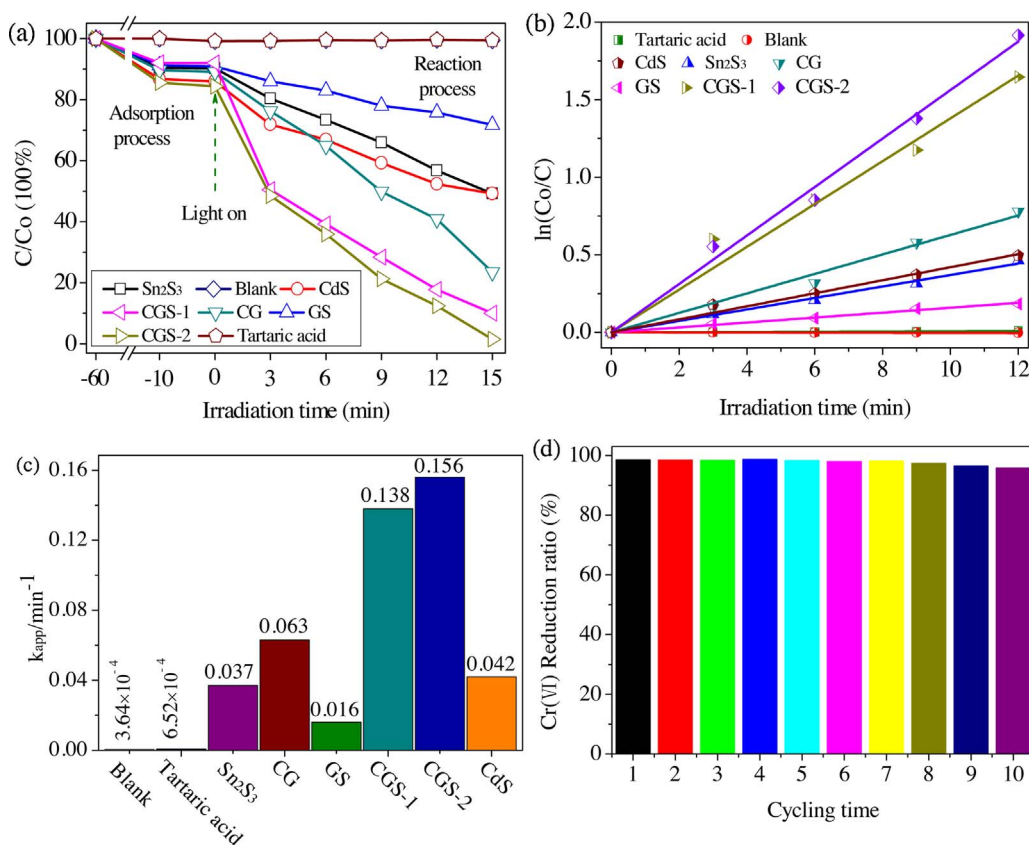


Fig. 4. (a) Visible light photoreduction of 100 mg L<sup>-1</sup> K<sub>2</sub>Cr<sub>2</sub>O<sub>7</sub> aqueous solution; (b) the reaction kinetics and (c) the apparent rate constants for photoreduction of aqueous Cr(VI) over various samples in the presence of 0.4 mol L<sup>-1</sup> tartaric acid; (d) Cycling photoreduction curves of CGS-2 sample under visible-light illumination ( $\lambda > 420$  nm).

Supporting information) and the used CGS-2 sample obtained after photocatalytic hydrogen evolution for 60 h (Fig. S9f; Supporting Information) demonstrate a similar doublet at binding energies of 486.8 and 495.2 eV, corresponding to Sn 3d<sub>5/2</sub> and Sn 3d<sub>3/2</sub>, respectively. Compared with the fresh CGS-2 sample, there are two extra peaks located at 72.2 and 75.4 eV in Pt 4f XPS spectrum of the used CGS-2 sample obtained after photocatalytic hydrogen evolution for 60 h (Fig. S9f; Supporting Information), which can be assigned to Pt 4f<sub>7/2</sub> and Pt 4f<sub>5/2</sub>, respectively, attributing to the formation of metallic Pt<sup>0</sup> during the photo-reduction process. As is known to all, XPS is a useful surface-sensitive technique, which can bring us some important surface information triggered by the structural reconfiguration. Most noteworthy is that the calculated atomic concentration of S and Sn elements in fresh CGS-2 sample are 1.08% and 0.56%, respectively, which are slightly larger than those of the used CGS-2 composites obtained after photocatalytic hydrogen evolution for 60 h (the calculated atomic concentration of S and Sn elements are only 0.80% and 0.17%, respectively). Conversely, the relatively atomic concentration of Cd element in fresh CGS-2 sample was 0.26%, while the calculated value of Cd element is as high as 0.54% for the used CGS-2 composites obtained after photocatalytic hydrogen evolution for 60 h. These results show that the content of CdS on the surface of the used CGS-2 composites obtained after photocatalytic hydrogen evolution for 60 h is higher than that of the fresh CGS-2 sample. On the contrary, the content of Sn<sub>2</sub>S<sub>3</sub> on the surface of the CdS-Sn<sub>2</sub>S<sub>3</sub>@rGO heterostructures decreased after photocatalytic hydrogen evolution for 60 h. These phenomena can be attributed to the fact that, benefiting from the photoreaction-driven structural restructuring behavior, a mass of Sn<sub>2</sub>S<sub>3</sub> nanocrystals covered on the surface of CdS tended to break up, thus resulting in the highly dispersed Sn<sub>2</sub>S<sub>3</sub> nanocrystals and more exposed CdS nanocrystals on the surface of CdS-Sn<sub>2</sub>S<sub>3</sub>@rGO heterostructures after photocatalytic hydrogen evolution reaction. The XPS analysis results further confirm the peculiarly structural reconfiguration effect occurred on the CdS-Sn<sub>2</sub>S<sub>3</sub>@rGO nanocomposite.

We also carried out the additional thermogravimetric analysis (TGA) and inductively coupled plasma atomic emission spectroscopy (ICP) measurement to investigate the stability of CdS-Sn<sub>2</sub>S<sub>3</sub>@rGO hybridized photocatalyst. As shown in Fig. 6a, TGA analyses were performed on both the fresh CGS-2 composites and the used CGS-2 composites after photocatalytic hydrogen evolution for 6 h from ambient temperature to 800 °C at a heating rate of 10 °C min<sup>-1</sup>. Due to the influence of nitrogen flow disturbance, we can observe the phenomenon of overweight in the initial heating stage (30–150 °C) for the two samples. Obviously, the weight loss of fresh CGS-2 composites is calculated to be 24.2 wt.% at 700 °C due to the removal of the crystal water and the numerous oxygen-containing functional groups involved in graphene. However, the TGA curve of the used CGS-2 composites obtained after photocatalytic hydrogen evolution for 60 h exhibits an interesting three-step process: the first degradation step is from 150 to 447 °C, and the weight loss of sample is about 7.8 wt.% at 447 °C, due to the removal of the crystal water and the residual scavenger lactic acid as well as the part of oxygen-containing functional groups. Next, the TGA curve shows a gradual increase in mass during period of heat-up and the weight loss of sample is only about 3.5 wt.% at 550 °C, which is ascribed to the fact that the metallic Pt<sup>0</sup> was oxidized by the oxygen-containing functional groups and finally converted into platinum oxide (PtO<sub>2</sub>). In the third degradation step, the gradual decay of the TGA curve from around 550 °C to 700 °C represents that Sn<sub>2</sub>S<sub>3</sub> was gradually oxidized by the released oxygen-containing functional and transformed into the tin dioxide, thus leading to a weight loss of no more than 5.7 wt.% at 700 °C.

Furthermore, the concentration of Cd<sup>2+</sup> in aqueous solution was measured by ICP. Before the photocatalytic reaction, 66 mg of CGS-2 composites (the content of CdS is 42.24 mg in this sample) was dispersed in 60 mL deionized water which containing 10 mL lactic acid as electron donors. As demonstrated in Fig. 6b, after photocatalytic hydrogen evolution for 2 h, the concentration of Cd<sup>2+</sup> in the aqueous solution were measured to be 4.20 mg L<sup>-1</sup>, and the corresponding



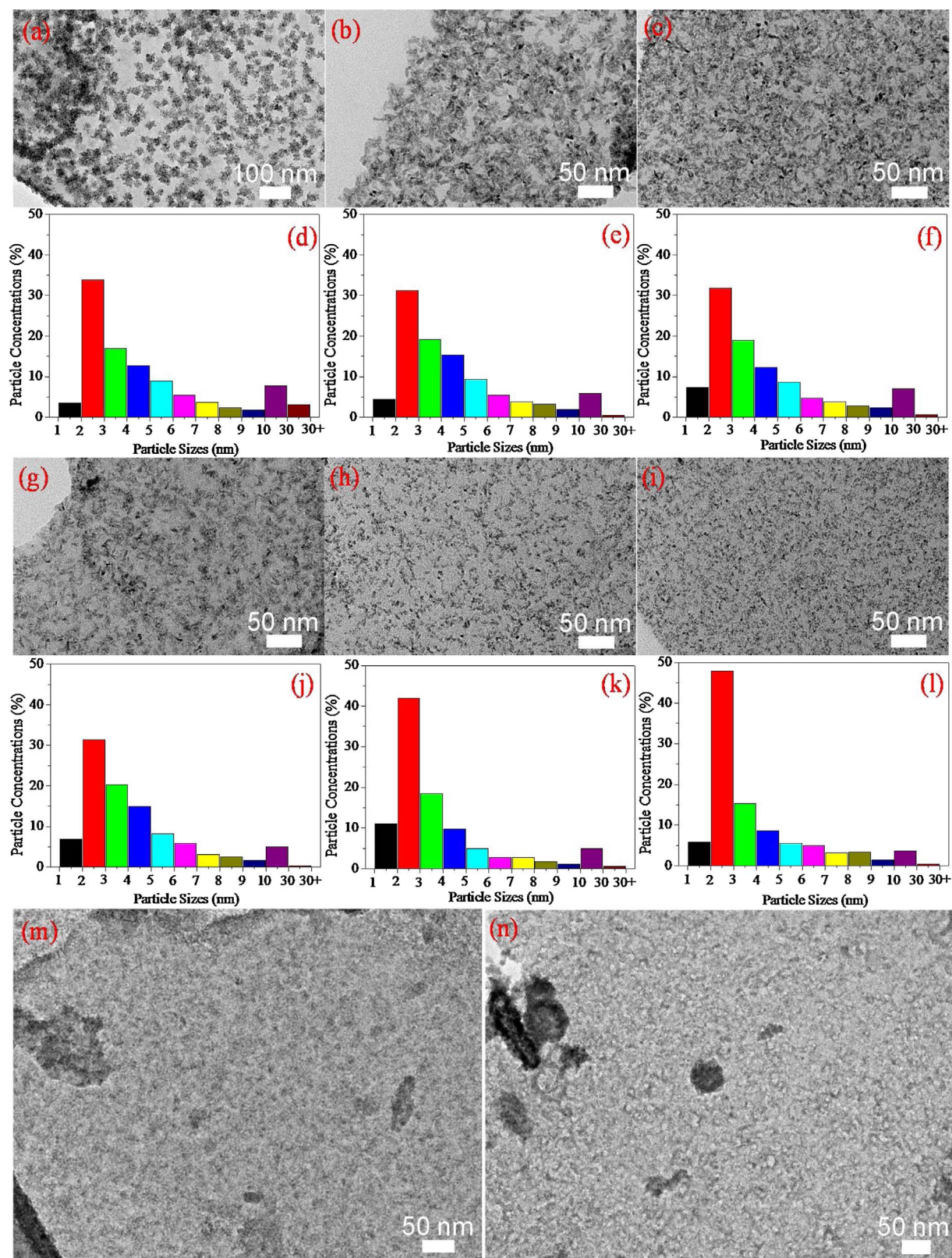
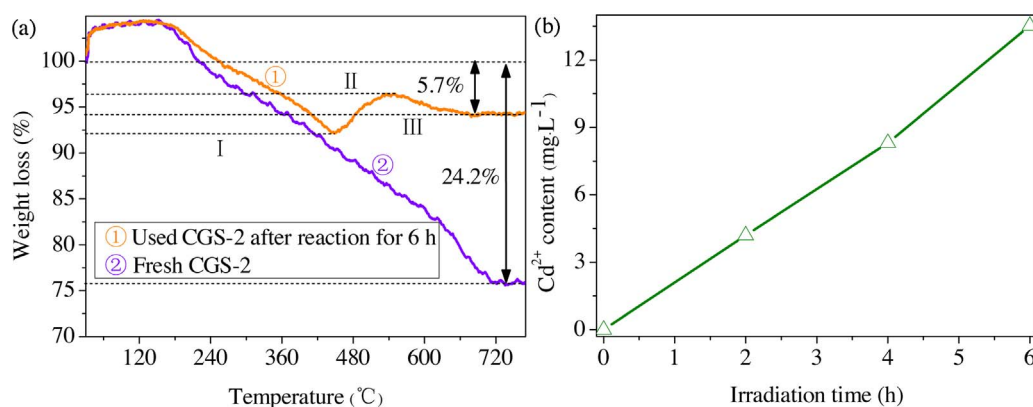


Fig. 5. TEM images of CGS-2 composites under photocatalytic reaction for (a) 0 h, (b) 1 h, (c) 2 h, (g) 3 h, (h) 4 h, (i) 5 h, (m) 6 h, (n) 60 h. Particle sizes distributions determined by TEM: (d) 0 h, (e) 1 h, (f) 2 h, (j) 3 h, (k) 4 h, (l) 5 h.

derived percentage of the dissolved CdS is only 0.76 wt.%. Under the visible light irradiation for 4 h, the concentration of  $\text{Cd}^{2+}$  in the aqueous solution slightly increased to  $8.31 \text{ mg L}^{-1}$ . It indicates that only 1.51 wt.% of CdS in the  $\text{CdS-Sn}_2\text{S}_3/\text{rGO}$  heterostructures was dissolved

into water during the photocatalytic reduction process. When the irradiation time is extended to 6 h, the calculated value of  $\text{Cd}^{2+}$  is  $13.53 \text{ mg L}^{-1}$ , corresponding to 2.46 wt.% of the dissolved CdS. Based on the above-mentioned data, it can be concluded that although the



**Fig. 6.** (a) TGA curves of the fresh CGS-2 composites and the used CGS-2 composites after photocatalytic hydrogen evolution for 6 h; (b) Time-dependent concentration of Cd<sup>2+</sup> in the aqueous solution over CGS-2 nanocomposites under irradiation with visible light ( $\lambda > 420$  nm).

drastic structural reconstruction was happened over the as-prepared CdS-Sn<sub>2</sub>S<sub>3</sub>@rGO heterostructures during the photocatalysis process, only a tiny fraction of CdS was dissolved in aqueous solutions after photocatalytic hydrogen evolution for 6 h, indicating that the CdS-Sn<sub>2</sub>S<sub>3</sub> eutectic cluster bonding on the surface of rGO nanosheets possessed excellent chemical stability, and the photocorrosion of CdS can be significantly inhibited in this kinds special graphene-based nanosheet photocatalysts.

Moreover, further evidence for the unusually photoreaction-driven structural reconstruction process of CdS-Sn<sub>2</sub>S<sub>3</sub> eutectic clusters comes from XRD patterns. As shown in Fig. 7a, the crystal structure of hexagonal CdS and orthorhombic Sn<sub>2</sub>S<sub>3</sub> in CGS-2 composite has no change with the photoreaction ongoing. However, the calculated crystal sizes of the orthorhombic Sn<sub>2</sub>S<sub>3</sub> showed obvious change, which decreased with the increase of reaction time. In contrast, the crystal sizes of the hexagonal CdS almost were unchanged (Table S1, Supporting Information). This phenomenon implies that the continuously restructuring was occurred in Sn<sub>2</sub>S<sub>3</sub> nanocluster, and thus the CdS-Sn<sub>2</sub>S<sub>3</sub>@rGO composite can serve as sustained-release tablets to induce the explosion of numerous active sites during the hydrogen evolution reaction process. Fig. 7 schematically illustrated the tentative mechanism of charge transfer and separation on CGS-2 composite before and after reconstruction. As shown in Fig. 7c, before the photoreduction, the fresh CGS-2 composite shows a typical graphene nanosheet structure, and a mass of Sn<sub>2</sub>S<sub>3</sub> nanocrystals intertwined and covered on the surface of CdS to self-assembly macroaggregated CdS-Sn<sub>2</sub>S<sub>3</sub> eutectic clusters with a large diameter ranging from 16.7 nm to 27.8 nm, which thus seriously hindered the light absorption and generation of photo-induced electrons and holes inside CdS. Furthermore, the aggregation effect of the large CdS-Sn<sub>2</sub>S<sub>3</sub> particles not only led to a longish geometrical charge transfer pathways in CdS particles, but also resulted in low interfacial contact efficiency with 2D surface. It is believed that all the above-mentioned disadvantages severely hampered the charge carrier migration and separation in CGS-2 composites, and thus leading to a relatively low photocatalytic activity in the early stage of H<sub>2</sub> generation from water splitting. However, under continuous illumination, the local photothermal effect of graphene triggered off significantly structural restructuring of CdS-Sn<sub>2</sub>S<sub>3</sub> eutectic clusters locating on the rGO nanosheets. According to the aforementioned TEM (Figs. 5b–n and 7d) and XRD analyses, the cocatalyst Sn<sub>2</sub>S<sub>3</sub> nanocrystals underwent dramatic and irreversible structural restructuring. Benefiting from its intriguing structural restructuring behavior, the isolated CdS-Sn<sub>2</sub>S<sub>3</sub> eutectic clusters tended to break up. Thus, a growing number of cocatalysts Sn<sub>2</sub>S<sub>3</sub> with smaller crystal size and tiny CdS nanocrystals eventually scattered throughout the whole rGO platform to form the effective metal sulfides-graphene interfacial contact, respectively, resulting in more exposed CdS light-adsorption sites and Sn<sub>2</sub>S<sub>3</sub> reactive sites [7]. Attributing to the short charge carrier diffusion length (below 10 nm) derived from smaller particle size, the photo-induced electrons and holes can easily migrate to the surface of CdS, thus decreasing the

probability of charge carrier recombination inside CdS [35]. What's more, the introduced few-layer rGO nanosheets not only are an ideal support for semiconductor loading, but also act as an efficient electron acceptor and charge transfer bridge, owing to the lower Fermi level of rGO (-0.08 eV vs. NHE) [36–41]. Therefore, the accumulated electrons at the CdS edge can vectorially transfer from CdS to the rGO framework and ultimately migrate to the dual cocatalysts of Sn<sub>2</sub>S<sub>3</sub> and Pt nanoparticles via the constructed interfacial heterojunctions (red dashed line in Fig. 7d), accompanied with the quenching of the photo-induced holes by the scavenger of lactic acid. And the prolonged lifetime of photo-induced charge carriers can be further confirmed by time-resolved photoluminescence spectra (Fig. 7b) [42–46]. Overall, it can be concluded that the unusually photoreaction-driven structural reconfiguration of CdS-Sn<sub>2</sub>S<sub>3</sub> eutectic clusters on rGO nanosheets has a significant impact in engineering CdS-Sn<sub>2</sub>S<sub>3</sub>@rGO composites with highly-efficient interfacial charges separation and transfer, thereby leading to a substantially enhanced photocatalytic performance, as well as the stability. This positive effect has already been robustly demonstrated by the visible-light photocatalytic H<sub>2</sub> evolution over CGS-2 composites, which displays much higher H<sub>2</sub> evolution rate (1671  $\mu\text{mol h}^{-1} \text{g}^{-1}$ ) after 10 cycles of intensive accelerated durability testing.

#### 4. Conclusions

In summary, we have reported a facile synthesis strategy for the large-scale fabrication of the ternary CdS-Sn<sub>2</sub>S<sub>3</sub>@rGO eutectic cluster heterostructures. Numerous CdS-Sn<sub>2</sub>S<sub>3</sub> eutectic clusters anchored onto rGO surfaces can be reconfigured during the photocatalytic reaction process, which acted as sustained-release system of active sites. The resultant CdS-Sn<sub>2</sub>S<sub>3</sub>@rGO eutectic cluster heterostructures exhibited high activity and stability both in photocatalytic H<sub>2</sub> evolution and Cr (VI) reduction under visible light irradiation. The combination of shorter charge-transfer distance, the effective interfacial contact, superior electrical conductivity of rGO and ever-increasing surface reactive sites efficiently promote the separation and transfer of photo-generated electron-hole pairs, thus endow CdS-Sn<sub>2</sub>S<sub>3</sub>@rGO heterostructures with the formidably superior durability in photo-reduction reaction process. We envision that our research will provide new insight into the design of nanoarchitectures with high activity for environmental remediation and solar hydrogen generation.

#### Acknowledgments

This work was financially supported by the Natural Science Basic Research Plan in Shaanxi Province of China (Grant No. 2017JZ001), the National Natural Science Foundation of China (Grant No. 21303130), State Key Laboratory of Heavy Oil Processing (Grant No. SKLOP201602001), the Fundamental Research Funds for the Central Universities (Grant No. cxt2017004) and the Open Fund of the State Key Laboratory of Luminescent Materials and Devices (South China



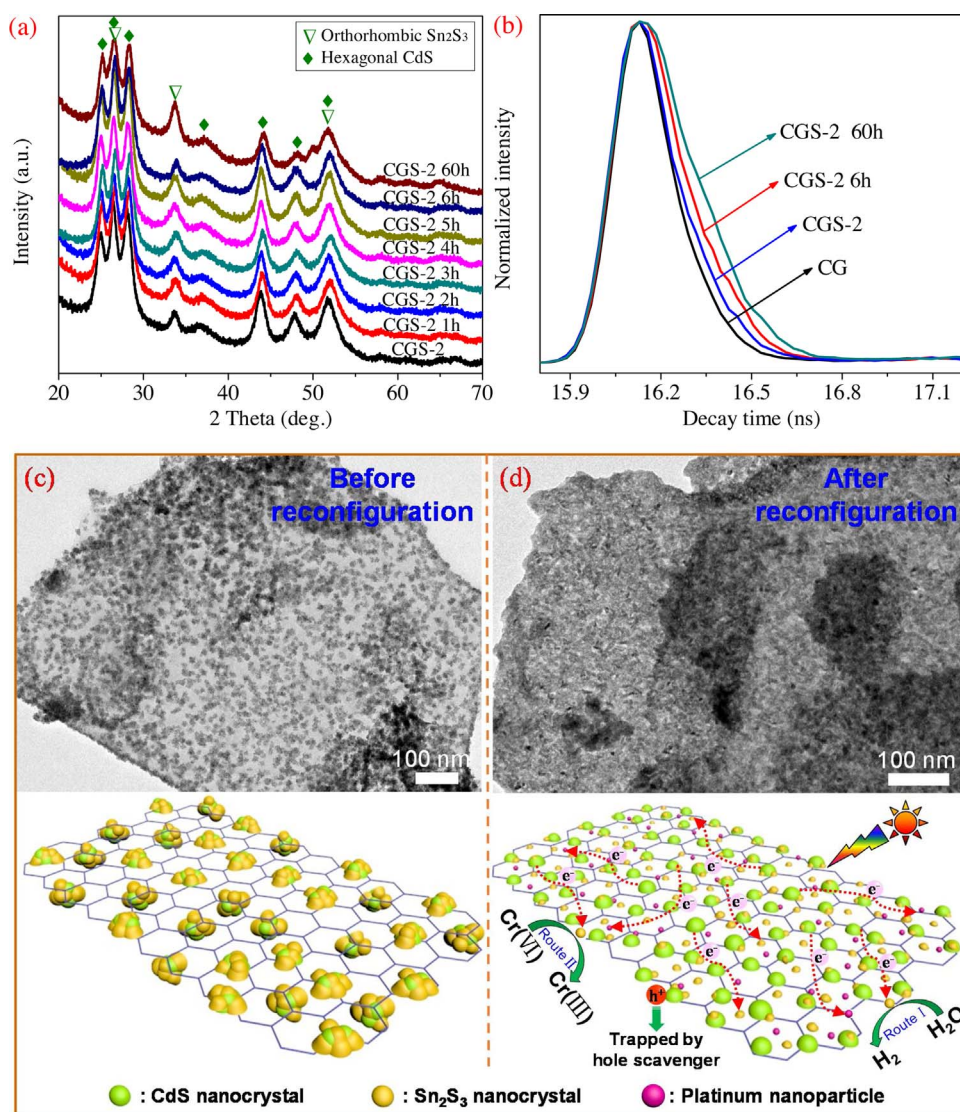


Fig. 7. (a) XRD patterns and (b) time-resolved PL spectra (excitation wavelength: 425 nm) of various samples during photocatalytic  $H_2$  evolution reaction at different time; Schematic of the charge transfer and separation for CGS-2 composite under photocatalytic reactions for (c) 0 h and (d) 60 h.

University of Technology, Grant No. 2016-skllmd-04). Thanks for the technical support from International Center for Dielectric Research (ICDR), Xi'an Jiaotong University, Xi'an, China; the authors also appreciate Ms. Dai and Mr. Ma for their help in using SEM, EDX and TEM, respectively.

## Appendix A. Supplementary data

Supplementary data associated with this article can be found, in the online version, at <http://dx.doi.org/10.1016/j.apcatb.2017.10.008>.

## References

- [1] L. Foppa, C. Copéret, A. Comas-Vives, *J. Am. Chem. Soc.* 138 (2016) 16655–16668.
- [2] V. Ledentu, W. Dong, P. Sautet, *J. Am. Chem. Soc.* 122 (2000) 1796–1801.
- [3] D. Teschner, J. Borsodi, A. Wootsch, Z. Révay, M. Hävecker, A. Knop-Gericke, S.D. Jackson, R. Schlögl, *Science* 320 (2008) 86–89.
- [4] F. Tao, S. Dag, L.-W. Wang, Z. Liu, D.R. Butcher, H. Blum, M. Salmeron, G.A. Somorjai, *Science* 327 (2010) 850–853.
- [5] F. Tao, M.E. Grass, Y. Zhang, D.R. Butcher, J.R. Renzas, Z. Liu, J.Y. Chung, B.S. Mun, M. Salmeron, G.A. Somorjai, *Science* 322 (2008) 932–934.
- [6] F.F. Tao, M. Salmeron, *Science* 331 (2011) 171–174.
- [7] J. Ran, J. Zhang, J. Yu, M. Jaroniec, S.Z. Qiao, *Chem. Soc. Rev.* 43 (2014) 7787–7812.
- [8] F. Ma, H.B. Wu, B.Y. Xia, C. Xu, X.W.D. Lou, *Angew. Chem. Int. Ed.* 54 (2015) 15395–15399.
- [9] T. Hisatomi, J. Kubota, K. Domen, *Chem. Soc. Rev.* 43 (2014) 7520–7535.
- [10] Q. Xiang, B. Cheng, J. Yu, *Angew. Chem. Int. Ed.* 54 (2015) 11350–11366.
- [11] R. Bera, S. Kundu, A. Patra, *ACS Appl. Mater. Interfaces* 7 (2015) 13251–13259.
- [12] Q. Li, H. Meng, P. Zhou, Y. Zheng, J. Wang, J. Yu, J. Gong, *ACS Catal.* 3 (2013) 882–889.
- [13] S. Bai, W. Yin, L. Wang, Z. Lia, Y. Xiong, *RSC Adv.* 6 (2016) 57446–57463.
- [14] S. Min, G. Lu, *J. Phys. Chem. C* 115 (2011) 13938–13945.
- [15] Z. Yi, J. Ye, N. Kikugawa, T. Kako, S. Ouyang, H. Stuart-Williams, H. Yang, J. Cao, W. Luo, Z. Li, Y. Liu, R.L. Withers, *Nat. Mater.* 9 (2010) 559–564.
- [16] M. Liu, R. Zhang, W. Chen, *Chem. Rev.* 114 (2014) 5117–5160.
- [17] Q. Xiang, F. Cheng, D. Lang, *ChemSusChem* 9 (2016) 996–1002.
- [18] S. Peng, L. Li, X. Han, W. Sun, M. Srinivasan, S.G. Mhaisalkar, F. Cheng, Q. Yan, J. Chen, S. Ramakrishna, *Angew. Chem. Int. Ed.* 126 (2014) 12802–12807.
- [19] Z. Song, W. Li, F. Niu, Y. Xu, L. Niu, W. Yang, Y. Wang, J. Liu, *J. Mater. Chem. A* 5 (2017) 230–239.
- [20] M. Sun, H. Liu, Y. Liu, J. Qu, J. Li, *Nanoscale* 7 (2015) 1250–1269.
- [21] J. Hou, C. Yang, H. Cheng, Z. Wang, S. Jiao, H. Zhu, *Phys. Chem. Chem. Phys.* 15 (2013) 15660–15668.
- [22] M. Liu, F. Li, Z. Sun, L. Ma, L. Xu, Y. Wang, *Chem. Commun.* 50 (2014) 11004–11007.
- [23] Y. Jiang, M. Wei, J. Feng, Y. Ma, S. Xiong, *Energy Environ. Sci.* 9 (2016) 1430–1438.
- [24] T. Jia, A. Kolpin, C. Ma, R.C. Chan, W. Kwok, S.C.E. Tsang, *Chem. Commun.* 50 (2014) 1185–1188.
- [25] K.Y. Cho, Y.S. Yeom, H.Y. Seo, P. Kumar, K. Baek, H.G. Yoon, *J. Mater. Chem. A* (2017), <http://dx.doi.org/10.1039/c6ta09345k>.
- [26] W. Tu, Y. Zhou, Q. Liu, S. Yan, S. Bao, X. Wang, M. Xiao, Z. Zou, *Adv. Funct. Mater.* 23 (2013) 1743–1749.
- [27] J. Chen, X. Wu, L. Yin, B. Li, X. Hong, Z. Fan, B. Chen, C. Xue, H. Zhang, *Angew. Chem. Int. Ed.* 54 (2015) 1210–1214.
- [28] K. Lv, S. Fang, L. Si, Y. Xia, W. Ho, M. Li, *Appl. Surf. Sci.* 391 (2017) 218–227.
- [29] J. Zhang, W. Li, Y. Li, L. Zhong, C. Xu, *Appl. Catal. B—Environ.* 217 (2017) 30–36.
- [30] X. Hao, Z. Jin, H. Yang, G. Lu, Y. Bi, *Appl. Catal. B—Environ.* 210 (2017) 45–56.

- [31] S. Liu, M.-Q. Yang, Y.-J. Xu, J. Mater. Chem. A 2 (2014) 430–440.
- [32] J. Wang, X. Li, X. Li, J. Zhu, H. Li, Nanoscale 5 (2013) 1876–1881.
- [33] C. Xue, T. Zhang, S. Ding, J. Wei, G. Yang, ACS Appl. Mater. Interfaces 9 (19) (2017) 16091–16102.
- [34] X. Wu, L. Wen, K. Lv, K. Deng, D. Tang, H. Ye, D. Du, S. Liu, M. Li, Appl. Surf. Sci. 358 (2015) 130–136.
- [35] D.O. Sigle, L. Zhang, S. Ithurria, B. Dubertret, J.J. Baumberg, J. Phys. Chem. Lett. 6 (2015) 1099–1103.
- [36] Y. Xu, M. Kraftacd, R. Xu, Chem. Soc. Rev. 45 (2016) 3039–3052.
- [37] W. Jiang, Y. Liu, R. Zong, Z. Li, W. Yao, Y. Zhu, J. Mater. Chem. A 3 (2015) 18406–18412.
- [38] X. Long, J. Li, S. Xiao, K. Yan, Z. Wang, H. Chen, S. Yang, Angew. Chem. Int. Ed. 53 (2014) 7584–7588.
- [39] Y. Hou, A.B. Laursen, J. Zhang, G. Zhang, Y. Zhu, X. Wang, S. Dahl, I. Chorkendorff, Angew. Chem. Int. Ed. 52 (2013) 3621–3625.
- [40] W.-J. Ong, L.-L. Tan, S.-P. Chaia, S.-T. Yong, A.R. Mohamed, Nano Energy 13 (2015) 757–770.
- [41] X. Yu, J. Zhang, Z. Zhao, W. Guo, J. Qiu, X. Mou, A. Li, J.P. Claverie, H. Liu, Nano Energy 16 (2015) 207–217.
- [42] Y.P. Xie, Z.B. Yu, G. Liu, X.L. Ma, H.-M. Cheng, Energy Environ. Sci. 7 (2014) 1895–1901.
- [43] B. Lin, H. An, X. Yan, T. Zhang, J. Wei, G. Yang, Appl. Catal. B—Environ. 210 (2017) 173–183.
- [44] X. Guo, G. Zhang, H. Cui, N. Wei, X. Song, J. Li, J. Tian, Appl. Catal. B—Environ. 217 (2017) 12–20.
- [45] B. Lin, H. Li, H. An, W. Hao, J. Wei, Y. Dai, C. Ma, G. Yang, Appl. Catal. B—Environ. 220 (2018) 542–552.
- [46] C. Xue, H. An, X. Yan, J. Li, B. Yang, J. Wei, G. Yang, Nano Energy 39 (2017) 513–523.